

# Bidirectional Targeted Therapy Enables Efficient, Stable, and Eco-Friendly Perovskite Solar Cells

Xingnan Qi, Chongping Song, Weihai Zhang, Yueqing Shi, Yueyue Gao,\* Heng Liu, Rui Chen, Luwen Shang, Hairen Tan,\* Furui Tan,\* and Hsing-Lin Wang\*

Perovskite solar cells (PSCs) have witnessed rapid development toward commercialization based on their superior efficiency except for some remained misgivings about their poor stability primarily originating from interfacial problems. Robust back interface for neutralization of crystal defects, depression of dopant lithium ions ( $\text{Li}^+$ ) diffusion, and even inhibition of toxic lead (Pb) leakage is highly desirable; however, it remains a great challenge. Herein, a cost-effective interfacial therapy approach is developed to simultaneously alleviate the obstacles aforementioned. A small molecule, 1,4-dithiane with unique chair structure, is adapted to interact with under-coordinated  $\text{Pb}^{2+}$  on perovskite surface and  $\text{Li}^+$  from hole transport layer, neutralizing interfacial defects and suppressing  $\text{Li}^+$  diffusion. Besides, the presence of 1,4-dithiane can efficiently modulate interfacial energetics, enhance hydrophobicity of PSCs, and anchor Pb atoms via S–Pb bond. Consequently, the target devices perform better than control devices when exposed to light-soaking, moisture, and thermal stress owing to the synergistic suppression of trap-state density, ions migration, and moisture permeation. The optimized target device delivers a champion efficiency of 23.27% with mitigated Pb leakage. This study demonstrates a promising functionalized modification strategy for constructing efficient, stable, and eco-friendly PSCs.

figure-of-merits of derived perovskite material, i.e., large absorption coefficient, low exciton binding energy, and high charge carrier mobility, et al.<sup>[6–7]</sup> Up to now, the record efficiency of PSCs has exceeded 25%, which is benefited from great endeavors in device optimization and in-depth mechanism investigation.<sup>[8–9]</sup>

In spite of significant progress having been achieved for PSCs, their practical application is still hindered by their poor stability. On the one hand, the solution-processed perovskite film is composed of polycrystalline grains, inevitably inducing a large number of structural defects, especially those under-coordinated lead ions ( $\text{Pb}^{2+}$ ).<sup>[10]</sup> On the other hand, most reported high-performance PSCs are assembled via lithium ions ( $\text{Li}^+$ ) doped Spiro-OMeTAD as hole transport layer (HTL), in which  $\text{Li}^+$  ions would gradually diffuse across the perovskite layer for its small radius and high diffusion rate.<sup>[11]</sup> Consequently, those intrinsic defects and external ions migration would lead to the

decomposition of perovskite layer after long-term operation or undergoing severe stresses, resulting in the degradation of device performance and increasing the potential risk of toxic Pb leakage to the ambient environment.<sup>[12–13]</sup> Therefore, developing robust strategy to holistically improve the device stability together with suppressed Pb leakage is of significant importance for the practical application of PSCs.

## 1. Introduction


The past decade has been witnessing the swift development of organic-inorganic lead-halide hybrid perovskite solar cells (PSCs), which are featured with low fabrication cost and excellent photovoltaic efficiency.<sup>[1–5]</sup> The superior photovoltaic performance of PSCs can be attributed to the favorable

X. Qi, C. Song, Y. Gao, L. Shang, F. Tan  
Key Laboratory of Photovoltaic Materials  
Henan University  
Kaifeng 475004, P. R. China  
E-mail: gaoyueyue@henu.edu.cn; firtan@henu.edu.cn

X. Qi, W. Zhang, H. Liu, H.-L. Wang  
Key University Laboratory of Highly Efficient Utilization of Solar Energy and Sustainable Development of Guangdong  
Department of Materials Science and Engineering  
Southern University of Science and Technology  
Shenzhen 518055, P. R. China  
E-mail: wangxl3@sustech.edu.cn

Y. Shi, R. Chen  
Department of Electrical and Electronic Engineering  
Southern University of Science and Technology  
Shenzhen 518055, P. R. China

H. Tan  
National Laboratory of Solid State Microstructures  
Collaborative Innovation Center of Advanced Microstructures  
Jiangsu Key Laboratory of Artificial Functional Materials College of Engineering and Applied Sciences  
Nanjing University  
Nanjing 210093, P. R. China  
E-mail: hairentan@nju.edu.cn

 The ORCID identification number(s) for the author(s) of this article can be found under <https://doi.org/10.1002/adfm.202214714>.

DOI: 10.1002/adfm.202214714

To date, interfacial post-treatment upon perovskite film via organic molecules, i.e., alkylammonium halides, ionic liquid, and polymers et al., has been reported as an effective method to neutralize those notorious under-coordinated  $\text{Pb}^{2+}$  distributed on perovskite surface, contributing to highly efficient PSCs.<sup>[14–16]</sup> Nevertheless, the stability of these post-treated PSCs is still far from satisfactory due to the external  $\text{Li}^+$  migration under operational conditions.<sup>[17]</sup> Comparatively, incorporating 2D transition metal dichalcogenide or crown ether to  $\text{Li}^+$  doped Spiro-OMeTAD HTL is reported to be effective to coordinate with  $\text{Li}^+$  and then suppress its migration.<sup>[18–19]</sup> However, the referenced approach is not able to benefit the conversion efficiency due to those remaining intrinsic defects in perovskite layer.<sup>[20]</sup> Importantly, the potential Pb leakage from the photoactive layer was commonly ignored in those works. And the environmental problem remains to be a concern that hinders PSCs toward scalable civilian usage.<sup>[21–22]</sup> Thus, to fabricate efficient, stable, and eco-friendly PSCs, it is imperative but challenging to select interfacial materials for simultaneously resolving those critical interfacial problems including  $\text{Li}^+$  ions diffusion, Pb leakage as well as defect passivation.

Herein, an easily accessible yet cost-effective strategy is developed to alleviate the three remaining problems: we construct a bidirectionally targeted therapy approach to the perovskite/HTL interface by introducing a chair-structured small molecule (1,4-dithiane). It is noticed that 1,4-dithiane can simultaneously interact with under-coordinated  $\text{Pb}^{2+}$  distributed perovskite surface and  $\text{Li}^+$  ions from Spiro-OMeTAD HTL. Besides, the introduced 1,4-dithiane layer is able to fine-tune the interfacial energetics, enhance hydrophobicity of the resulting PSCs, and anchor Pb atom via S–Pb bond. Profiting from this multifunctional interfacial layer, the resulting target devices yield a champion efficiency of 23.27% together with the significantly improved stability against light-soaking, moisture, and thermal stresses. More importantly, the optimized target device exhibits improved eco-compatibility with almost 50% reduction of Pb leakage probability versus the control device.

## 2. Results and Discussion

Figure 1a depicts the chemical structure of 1,4-dithiane, which preferentially adopts a chair mode (−35.05 eV) rather than boat mode (−34.18 eV) for the relatively smaller energy of the former. Besides, the simulated electrostatic surface potential (ESP) of 1,4-dithiane shows that the negative potential and the positive potential mainly populate at its sulfur atoms and carbon/hydrogen atoms, respectively. The electron-rich characteristic of sulfur atoms can enable 1,4-dithiane as a Lewis base to form strong interaction with  $\text{Li}^+$  and  $\text{Pb}^{2+}$ , which is corroborated by the shortened bond length of S–Li (2.39 Å) and S–Pb (2.74 Å) compared to the derived sum of van der Waals radius of S–Li (2.56 Å) and S–Pb (3.13 Å), respectively, as summarized in Table S1 (Supporting Information).<sup>[23–25]</sup> Besides, the negative yet low binding energy S–Li (−0.95 eV) and S–Pb (−3.61 eV) definitely confirm the interaction between 1,4-dithiane and  $\text{Li}^+/\text{Pb}^{2+}$  (Figure 1b).<sup>[26]</sup> In addition, the Lewis acid feature of C–H from 1,4-dithiane enables it to form hydrogen bonds with  $\text{I}^-$  and formamidine (FA), which is confirmed by the corresponding shortened bond length as well as the reduced binding energy (Figure 1b; Figure S1 and Table S2, Supporting Information). Moreover, the variation of  $^1\text{H-NMR}$  spectrum of the FAI/1,4-dithiane complex relative to that of the individual FAI and 1,4-dithiane definitely demonstrates the formed hydrogen bond between FAI and 1,4-dithiane (Figure S2, Supporting Information).<sup>[27]</sup> Therefore, the chair-structure 1,4-dithiane should be energetically favorable to drive its bidirectional coordination with  $\text{Li}^+$  from HTL and under-coordinated  $\text{Pb}^{2+}$  as well as  $\text{I}^-$  distributed on perovskite surface (Figure 1c). The holistical interaction of 1,4-dithiane could be expected to suppress external  $\text{Li}^+$  migration and neutralize the intrinsic defects of perovskite, which is essential for constructing efficient PSCs. Moreover, the thermal stability of perovskite film modified via 1,4-dithiane is definitely enhanced due to the interaction between 1,4-dithiane and FAI, which is intuitively confirmed by the color change and the derived XRD pattern of modified perovskite film versus the pristine one when suffering from continuous thermal stress (225 °C, Figure S3, Supporting Information).

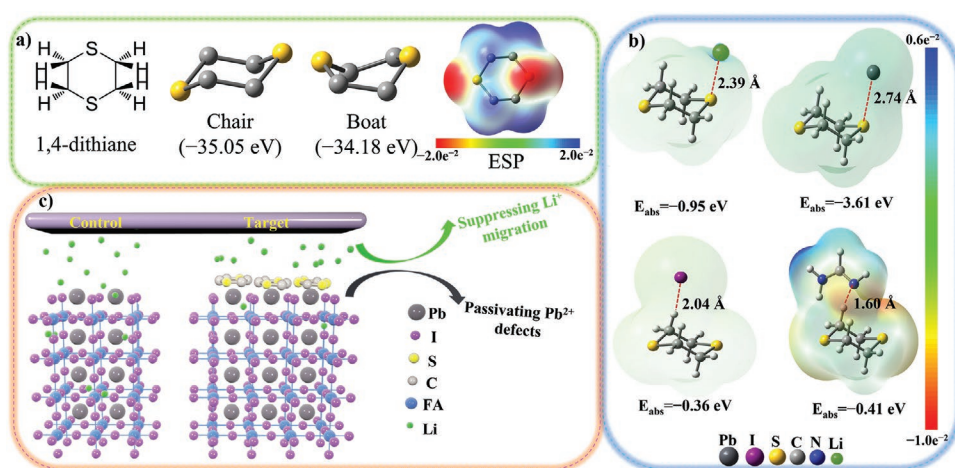


**Figure 1.** a) The molecular structure of 1,4-dithiane, the molecular geometry and electrostatic surface potential obtained from DFT calculation; b) The binding energy between 1,4-dithiane and different ions obtained from DFT calculation; c) The schematic diagram of the role of 1,4-dithiane on PSCs in this work.

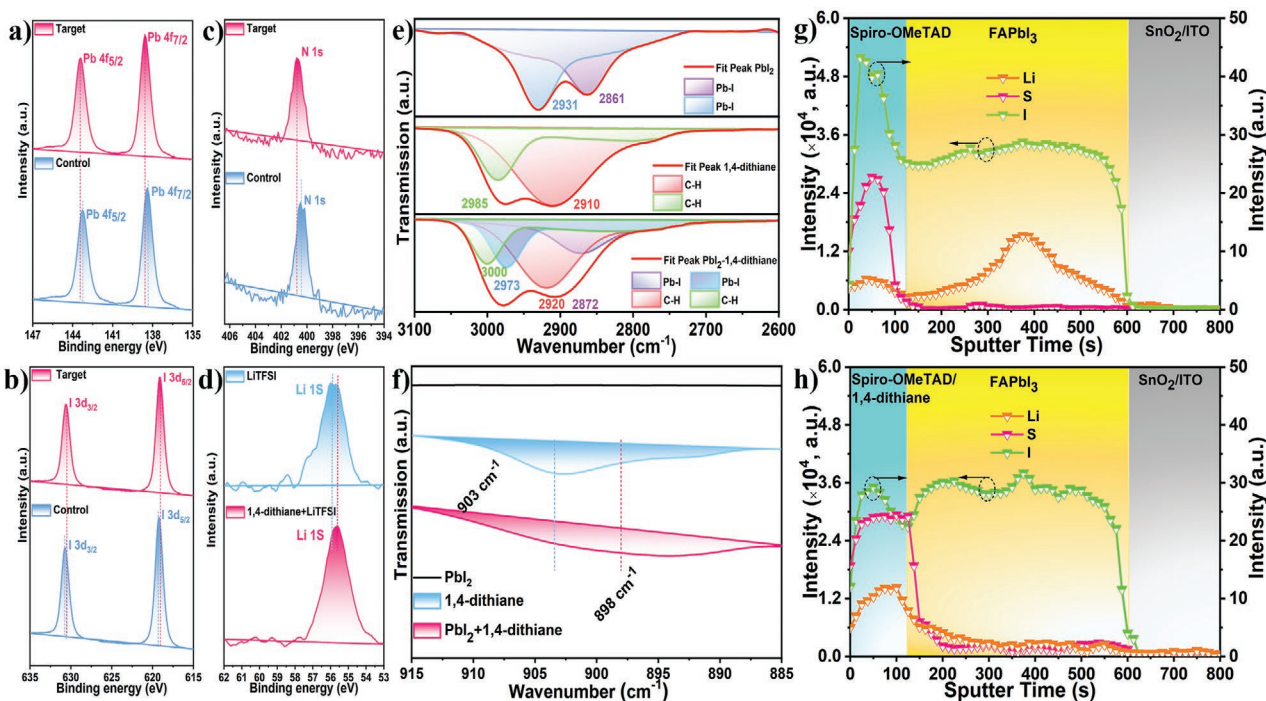


**Figure 2.** XPS spectra of a) Pb element, b) I element, c) N element, and d) Li element; FTIR spectra of different solutions for e) Pb–I bond and C–H bond and f) C–S bond; TOF-SIMS depth profiles of Li, I, and S element in (g) control device and (h) target device after light-soaking in ambient environment for 300 h.

To validate the interaction between 1,4-dithiane and  $\text{Li}^+/\text{Pb}^{2+}$ , the chemical environment of the film modified with (target) and without (control) 1,4-dithiane was investigated using X-ray photoelectron spectroscopy (XPS). Noted that the presence of sulfur signal in the XPS survey spectra (Figure S4, Supporting Information) and energy-dispersive X-ray spectroscopy (EDS, Figure S5, Supporting Information) for the target film suggest that 1,4-dithiane is present yet homogeneously distributed on the surface of the target perovskite film. As shown in Figure 2a, the core XPS spectra of the control film exhibit distinct doublet peaks at 138.4 and 143.3 eV, which are ascribed to the binding energy of the  $\text{Pb } 4f_{7/2}$  and  $\text{Pb } 4f_{5/2}$ , respectively.<sup>[28]</sup> Comparatively, the corresponding peaks of the target film shift toward higher binding energy to 138.6 and 143.5 eV, respectively. In contrast, the I 3d core spectra of the target film shift by 0.2 eV toward lower binding energy versus the control film (Figure 2b). The abovementioned inverse binding energy shift of Pb 4f peaks and I 3d peaks reveals 1,4-dithiane imparts synergistic passivation but with different interaction types with  $\text{Pb}^{2+}$  and  $\text{I}^-$  distributed on the perovskite surface, which should be ascribed to dual features of 1,4-dithiane as Lewis base (sulfur sites) and Lewis acid (hydrogen sites).<sup>[29]</sup> Besides, the N 1s core spectra of the target film shift by 0.2 eV toward higher binding energy versus the control film (Figure 2c), indicating that 1,4-dithiane could stabilize organic components in perovskite via hydrogen bond ( $\text{N} \cdots \text{H}-\text{C}$ ), which is energetically favorable from DFT calculation and corroborated by the variation of the derived  $^1\text{H-NMR}$  spectra (Figure S2, Supporting Information).<sup>[30]</sup> In addition, the binding energy of Li 1s peaks from the lithium bis(trifluoromethanesulfonyl)imide (LiTFSI)/1,4-dithiane composition shifts by 0.3 eV toward lower binding energy

compared to the pure LiTFSI (Figure 2d; Figure S6, Supporting Information). Meanwhile, the Fourier transform infrared spectroscopy (FTIR) exhibits that the stretching vibration of C–S bond from 1,4-dithiane in LiTFSI/1,4-dithiane complex shifts to the lower wavenumber of 872  $\text{cm}^{-1}$  compared to that in pristine 1,4-dithiane (900  $\text{cm}^{-1}$ , Figure S7, Supporting Information).<sup>[31]</sup> The abovementioned results demonstrate that 1,4-dithiane can form coordination with  $\text{Li}^+$ , which is beneficial for stabilizing derived PSCs for the suppression  $\text{Li}^+$  migration.<sup>[32–33]</sup>

The interaction between 1,4-dithiane and perovskite was indirectly studied via the FTIR. As presented in Figure 2e, the stretching vibration of C–H bond in 1,4-dithiane presents positive shift from 2985/2910 to 3000/2920  $\text{cm}^{-1}$  in the 1,4-dithiane/ $\text{PbI}_2$  complex (Figure 2e).<sup>[34]</sup> Meanwhile, the stretching vibration of Pb–I bond in  $\text{PbI}_2$  shifts from 2931/2861  $\text{cm}^{-1}$  toward higher wavenumber of 2973/2872  $\text{cm}^{-1}$  (Figure 2e; Figure S8, Supporting Information). However, the stretching vibration of C–S bond in pure 1,4-dithiane shifts from 903  $\text{cm}^{-1}$  to lower wavenumber of 898  $\text{cm}^{-1}$  when complexed with  $\text{PbI}_2$  (Figure 2f).<sup>[31]</sup> The FTIR results indicate 1,4-dithiane can strongly interact with  $\text{PbI}_2$  through C–H and C–S bonds, which is in good agreement with the result of XPS and DFT calculation.

Furthermore, the time-of-flight secondary ion mass spectroscopy (TOF-SIMS) was implemented to study  $\text{I}^-$  and  $\text{Li}^+$  distribution.<sup>[35]</sup> Figure 2g,h exhibits the TOF-SIMS depth profiles of Li, S, and I elements in the control device and the target device after light-soaking in ambient environment (25–30 °C, 35–45% relative humidity) for 300 h. It is noteworthy that large amount of  $\text{Li}^+$  ions migrate from HTL to perovskite layer accompanied with some  $\text{I}^-$  ions diffusing into HTL (Figure 2g), which signifies the poor stability of the control device. While, after the

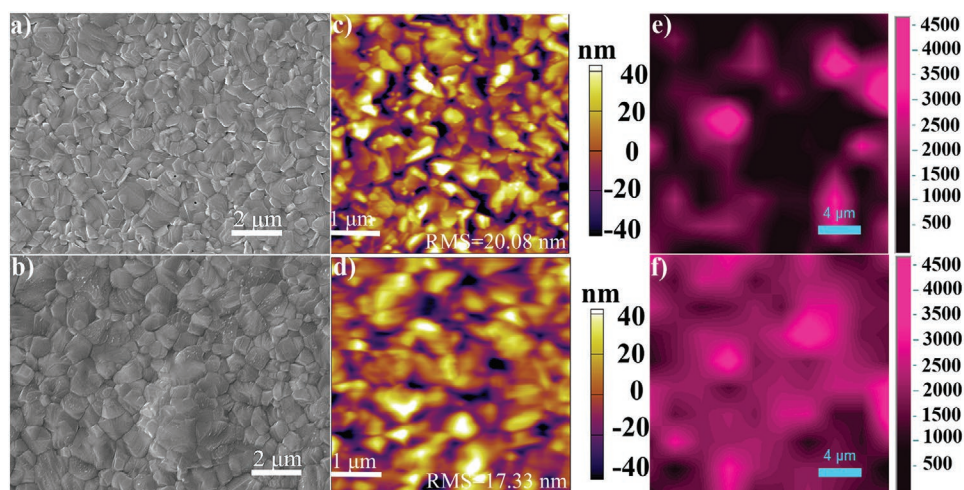


**Figure 3.** SEM image of a) control film and b) target film; AFM image of c) control film and d) target film; 2D PL mapping image of e) control film and f) target film.

introduction of 1,4-dithiane, the migration of  $\text{Li}^+$  ions from HTL to perovskite layer and the diffusion of  $\text{I}^-$  ions from perovskite layer into HTL are significantly reduced (Figure 2h), indicating that 1,4-dithiane can effectively suppress ions migration at the perovskite layer/HTL interface, which is conducive to improving the operational stability of derived PSCs.

Furthermore, the effect of 1,4-dithiane on the morphology and photophysical property of perovskite films was investigated. As shown in Figure 3a, the control film presents some pinholes along with heterogeneous grains distribution, which results in a rough surface with large root-mean-square roughness (RMS) of 20.08 nm (Figure 3c). In comparison, the target film shows compact and homogeneous grains distribution as well as a smooth surface (RMS = 17.33 nm, Figure 3b,d). The superior morphology of target film should be derived from its

better crystallinity, which is confirmed by its stronger X-ray diffraction intensity (Figure S9, Supporting Information). The higher quality of target film imparts enhanced absorption spectra versus the control film (Figure S10a, Supporting Information). Besides, the 2D photoluminescence (PL) mapping images reveal that the target film features a stronger and more homogeneous PL intensity distribution than the control one (Figure 3e,f), suggesting the suppressed non-radiative recombination for the reduced defect density in former, which is affirmed by decreased Urbach energy (Figure S10b, Supporting Information), enhanced steady-state PL intensity (Figure S10c, Supporting Information) and prolonged charge carrier lifespan in former (Figure S10d and Table S3, Supporting Information).<sup>[7]</sup>

Subsequently, the influence of 1,4-dithiane on the energetics of perovskite film was investigated. As shown in Figure 4a and

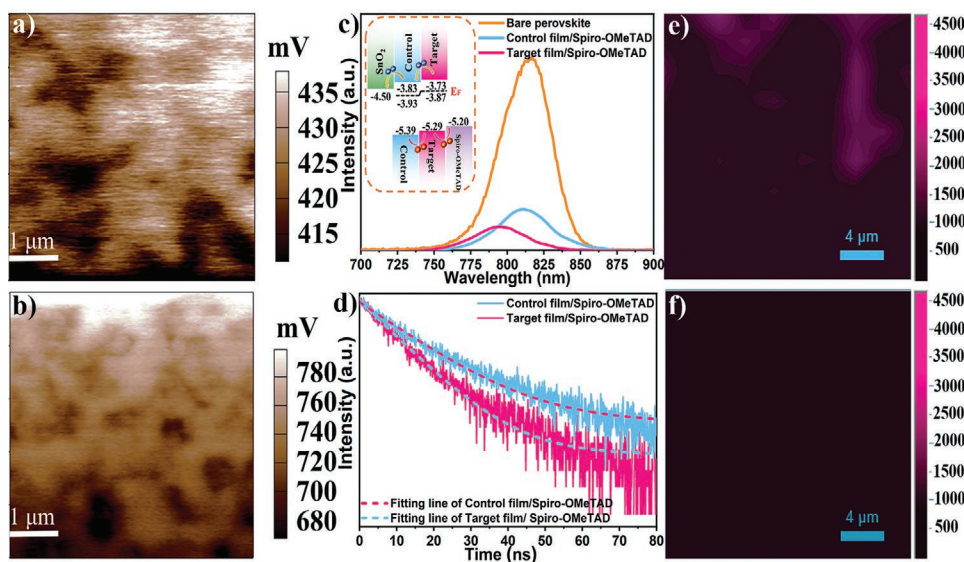


**Figure 4.** KPFM image of a) control film and b) target film; c) PL spectra and f) TRPL spectra of the pristine perovskite film, control film/HTL film, and target film/HTL film (note that the inset represents the energy level diagram of control film and target film); 2D PL mapping images of e) control film/HTL film and f) target film/HTL film.

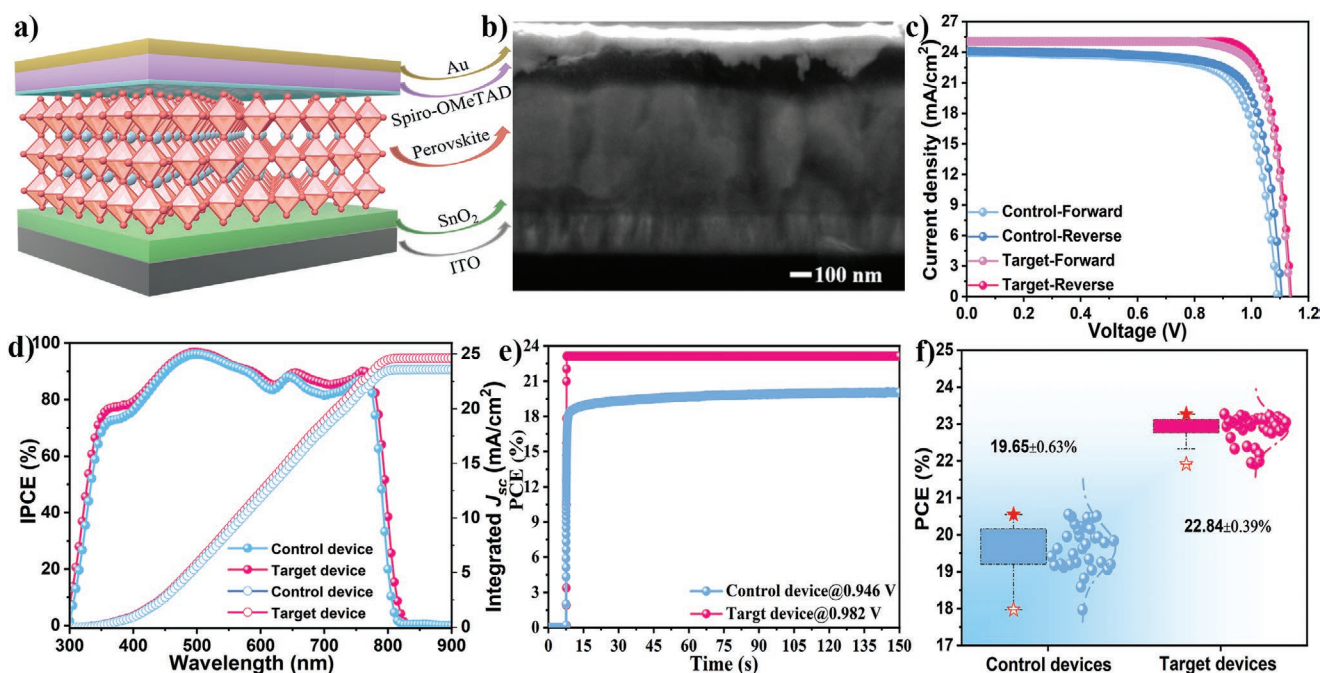


**Figure 5.** a) The schematic illustration of device architecture in this work; b) The cross sectional SEM image of champion target PSCs; c)  $J$ - $V$  curves of champion devices measured via reverse scan and forward scan; d) IPCE spectrum and corresponding  $J_{\text{int}}$  of champion devices; e) The SPO of champion devices; f) PCE histograms of champion devices from 34 individual cells.

Figure 4b, the Kelvin probe force microscopy (KPFM) image of the target film (Figure 4b) exhibits more homogeneous contact surface potential (CSP) distribution than that of the control one (Figure 4a), which benefits for photocarriers transfer in layer-stacked PSCs.<sup>[36]</sup> Besides, the average CSP value of the target film is almost increased by  $\approx 79\%$  versus that of the control one, which implies the smaller work function (WF) of the former and benefits for charge carrier extraction at the derived perovskite/HTL interface.<sup>[37]</sup>

UV photoelectron spectroscopy (UPS) was further applied to quantitatively evaluate the energetical variation of the perovskite film. As shown in the insert of Figure 4c as well as Figures S11–S13 (Supporting Information), the valence band maximum (VB), conduction band minimum (CB), Fermi level ( $E_f$ ), and middle band level ( $E_m$ ) of the control film are calculated to  $-5.39$ ,  $-3.83$ ,  $-3.93$ , and  $-4.61$  eV, respectively, calculated according to our previous work.<sup>[38]</sup> Compared to the control film, the derived energy levels of the target film up-shift to  $-5.29$ ,  $-3.73$ ,  $-3.87$ , and  $-4.51$  eV, respectively. Compared to the control film, the  $E_f$  of the target film relatively approaches its  $E_m$  yet shifts away from its CB, revealing a more intrinsic characteristic along with the mitigated  $n$ -type self-doping for the target film. The slightly weak  $n$ -type self-doping of the target film should be attributed to its reduced defect density due to the passivation effect of 1,4-dithiane and is beneficial for increasing the built-in potential and then reducing the risk of photogenerated holes backflow from HTL to perovskite layer, which contributes to improve the performance of PSCs with high fill factor (FF).<sup>[39,38]</sup> In addition, the upward-shifted CB of the target film could effectively block the undesirable reversed electron transfer occurring at the interface between perovskite and HTL.<sup>[40]</sup> Meanwhile, the minimized energy offset of 0.1 eV

between the target film and HTL could reduce energy loss of hole transfer in derived PSCs.<sup>[41]</sup>

To validate the enhanced hole extraction efficiency for the target film, the steady-state PL, the time-resolved PL, and 2D PL mapping was systematically conducted. As displayed in Figure 4c, the target film/HTL exhibits relatively higher PL quenching efficiency (88.6%) than that of the control film/HTL (79.3%), indicating that the hole extraction process is more efficient in former. Meanwhile, the maximum PL peak of the target film/HTL presents distinct blue shift versus that of the pristine perovskite film and the control film/HTL, coinciding well with the shift of the corresponding optical bandgap (Figure S14, Supporting Information), which should be ascribed to the healing upon the intra-bandgap defects of perovskite film due to the passivation of 1,4-dithiane.<sup>[42–44]</sup> Besides, the improved hole extraction process between the target film and HTL is confirmed by its shorter charge carrier lifetime (15.01 ns) than that for the control film/HTL (20.98 ns, Figure 4d; Table S4, Supporting Information). Moreover, the target film/HTL intuitively demonstrates more uniform yet complete PL quenching behavior than the control film/HTL (Figure 4e,f), further corroborating the enhanced hole extraction efficiency in former.<sup>[45,46]</sup> Overall, the 1,4-dithiane post-treatment upon perovskite film contributes to more favorable energetics for charge carrier extraction, thus benefiting for improving the photovoltaic performance of derived PSCs.

To confirm the effectiveness of 1,4-dithiane post-treatment on device performance, PSCs with planar configuration of ITO/SnO<sub>2</sub>/Perovskite/Spiro-OMeTAD/Au (Figure 5a) were fabricated. For maximizing the efficiency of corresponding devices, the concentration of 1,4-dithiane in isopropanol was carefully assessed, and the optimal concentration was determined at

**Table 1.** Photovoltaic properties of champion devices.

Devices	Scan direction	$V_{oc}$ [V]	$J_{sc}$ [mA cm <sup>-2</sup> ]	FF [%]	PCE <sub>max</sub> [%]	PCE <sub>average</sub> [%]	S	n
Control	FS <sup>a)</sup>	1.091	23.94	75.02	19.59	19.65 ± 0.63%	0.98	2.18
	RS <sup>b)</sup>	1.106	24.10	77.15	20.57			
Target	FS	1.136	25.03	80.85	22.99	22.84 ± 0.39%	0.99	1.77
	RS	1.140	25.11	81.32	23.27			

<sup>a)</sup>Forward scan and; <sup>b)</sup>Reverse scan.

0.3 mg mL<sup>-1</sup> (Figures S15, S16, and Table S5, Supporting Information). It is noted that the target perovskite film is vertically compact stacking between SnO<sub>2</sub> electron transport layer and Spiro-OMeTAD HTL (Figure 5b), being conducive to the vertical charge carrier transfer and extraction.<sup>[38]</sup> The current density–voltage (*J*–*V*) curves of champion devices are exhibited in Figure 5c and the corresponding photovoltaic parameters are listed in **Table 1**.

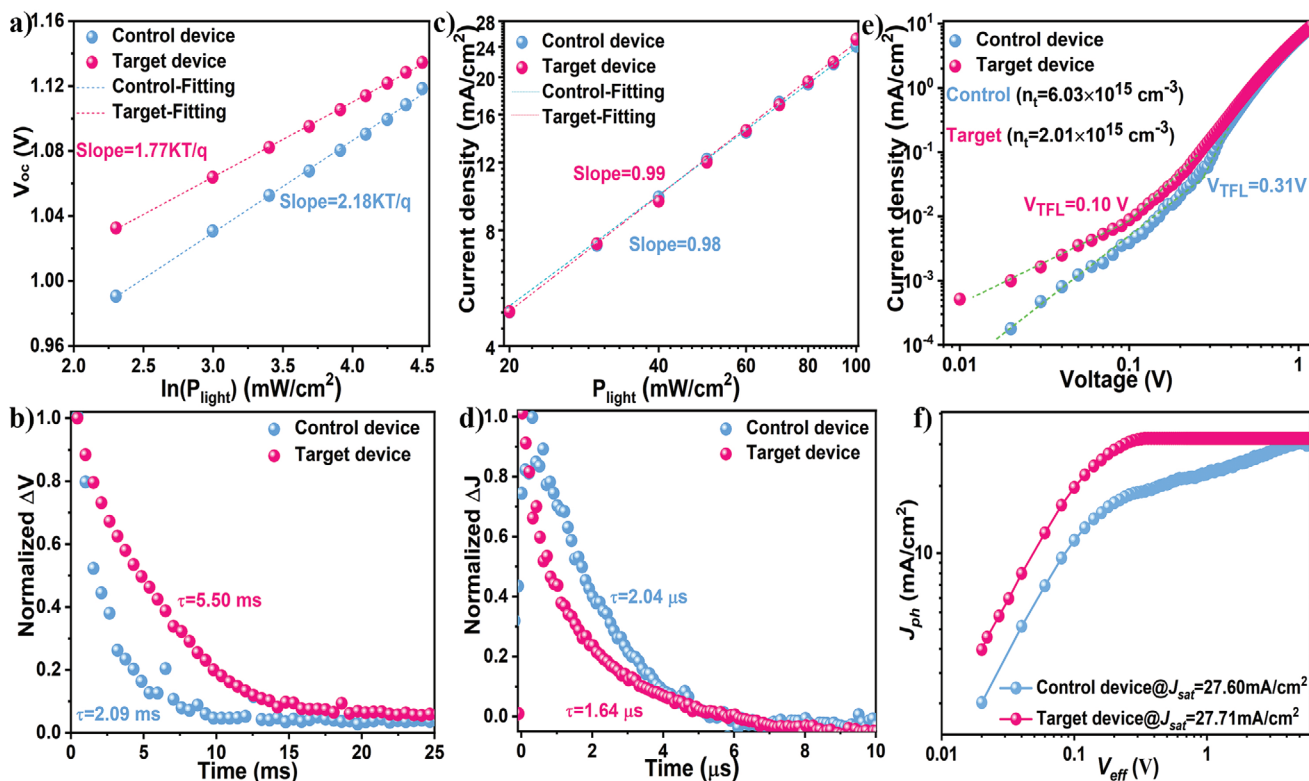
As exhibited in Figure 5c, the control device measured via reverse scan produces an open-circuit voltage ( $V_{oc}$ ) of 1.106 V, a short-circuit current density ( $J_{sc}$ ) of 24.10 mA cm<sup>-2</sup> and a FF of 77.17%, which produces a decent power conversion efficiency (PCE) of 20.57%. Comparatively, all photovoltaic parameters of the target device are increased with  $V_{oc}$  of 1.140 V,  $J_{sc}$  of 25.11 mA cm<sup>-2</sup>, and FF of 81.32%, delivering a remarkable PCE of 23.27%. Moreover, the target device shows a higher PCE of approaching 23.00% versus the control one (19.59%) when measured via the forward scan, eventually yielding a negligible hysteresis index (HI) of 0.012 compared to 0.048 for the control device. Moreover, the adaptability of this modification strategy is confirmed by the photovoltaic performance of MAPbI<sub>3</sub>-based devices. The modified MAPbI<sub>3</sub> device delivers a higher PCE of 20.82% along with a lower HI of 0.034 compared to the control device (18.23% and 0.142, Figures S17 and S18, and Tables S6 and S7, Supporting Information). It is noted that the champion photovoltaic performance of target devices (FAPbI<sub>3</sub> and MAPbI<sub>3</sub>) are both appreciable values among the derived PSCs featuring similar composition (Figures S19 and S20 and Tables S8 and S9, Supporting Information), demonstrating that the bidirectional targeted therapy strategy proposed in this work should be a promising avenue to assemble efficient yet reliable PSCs.

Figure 5d presents the incident photon-to-electron conversion efficiency (IPCE) spectra. The target device shows slightly stronger photon response during the visible region, resulting in a higher integrated current density ( $J_{int}$ ) of 24.62 mA cm<sup>-2</sup> than that of the control one (23.59 mA cm<sup>-2</sup>).<sup>[47]</sup> To further confirm the reliability of the *J*–*V* measurements, the steady-state power output (SPO) of devices at bias voltage near maximum power point (MPP) condition was recorded in Figure 5e. The SPO values of the control device and the target one are stabilized as 20.02% and 23.06%, respectively, which are consistent with the result of *J*–*V* curves of optimized devices, indicating the superiority of the target device relative to the control one. Moreover, the statistical histogram of target devices (22.84 ± 0.39%) from 34 individual cells reveals narrower PCE distribution than control devices (19.65 ± 0.63%, Figure 5f), corroborating an improved reproducibility yet superiority of the target devices.

To gain an in-depth understanding of the superior photovoltaic performance of target devices, the charge dynamics of champion devices were holistically studied. The  $V_{oc}$  as a function of light intensity ( $P_{light}$ ) was first recorded. Generally, the correlation between  $V_{oc}$  and  $P_{light}$  can be described as  $n = \frac{q}{KT} \frac{dV_{oc}}{d \ln P_{light}}$ , where  $q$ ,  $K$ ,  $T$ , and  $n$  represent electron charge, Boltzmann's constant, absolute temperature, and ideality factor, respectively.<sup>[48,49]</sup> And  $n$  has been applied to evaluate the charge carrier recombination behavior, where the derived value approaching unity indicates less trap-assisted recombination happening in devices. As exhibited in **Figure 6a**, the target device displays a lower  $n$  of 1.77 than the control one (2.18), suggesting that the trap-assisted recombination is significantly suppressed in former. Furthermore, the transient voltage (TPV) spectrum of the target device presents sluggish decay lifetime of 5.50 ms (Figure 6b) than the control one (2.09 ms), which further demonstrates that the charge recombination is effectively suppressed in former.<sup>[50–51]</sup>

As shown in Figure 6c, the target device depicts a larger exponential factor  $S$  of 0.99 derived from the equation ( $J_{sc} \propto P_{light}^S$ ) than the control device (0.98), signifying the faster charge extraction efficiency due to the favorable energy level alignment between the target film and HTL as discussed earlier.<sup>[52]</sup> Meanwhile, the target device exhibits a smaller transient photocurrent (TPC) decay lifetime of ≈1.64 μs (Figure 6d) than the control one of ≈2.04 μs, indicating an enhanced charge extraction efficiency, which is responsible for the higher  $J_{sc}$  of the former.<sup>[53]</sup>

Further, the trap-state density ( $N_t$ ) of the target film and the control one was calculated according to the equation  $N_t = \frac{2V_k \epsilon_r \epsilon_0}{qL^2}$ , where  $L$ ,  $\epsilon_r$ ,  $\epsilon_0$ , and  $V_k$  denote the thickness of the target film or the control one, the relative dielectric, the vacuum permittivity, and kink voltage between the ohmic-type region and the trap filling region, respectively.<sup>[54]</sup> As presented in Figure 6e, the target electron-only device preserves a smaller  $V_k$  of 0.10 V than the control one (0.31 V). Accordingly, the  $N_t$  of the target film and the control film are calculated to be  $2.01 \times 10^{15}$  and  $6.03 \times 10^{15}$  cm<sup>-3</sup>, respectively. The reduced  $N_t$  of the target film is beneficial for exciton dissociation and charge collection, which is corroborated by its higher photocurrent density ( $J_{ph}$ ) and larger saturation current density ( $J_{sat} = 2771$  mA cm<sup>-2</sup>, Figure 6f) than that of the control one ( $J_{sat} = 2760$  mA cm<sup>-2</sup>). Moreover, the superior exciton dissociation probability (90.6%) and charge collection efficiency (86.9%) of the target device relative to the control one (87.3% and 78.5%) further confirm that 1,4-dithiane post-treatment delivers more



**Figure 6.** a)  $V_{oc}$  values under different  $P_{light}$  for champion devices; b) TPV spectra of champion devices; c)  $J_{sc}$  values under different  $P_{light}$  for champion devices; d) TPC spectra of champion devices; e) The SCLC characterization of electron-only devices post-treated with or without 1,4-dithiane; f)  $J_{ph}$  versus effective voltage ( $V_{eff}$ ) of champion devices.

favorable charge dynamics for derived PSCs (Figure S21 and Table S10, Supporting Information).

Except for the device efficiency, the stability of PSCs is another critical concern for their practical application.<sup>[35,55]</sup> To reveal the positive effects of 1,4-dithiane post-treatment on the device stability, the PCE evolution of optimized devices under different environment was recorded. As shown in Figure S22 (Supporting Information), the unencapsulated target device shows considerably stable PCE evolution with 95.7% of its initial efficiency being retained after storing in an inert atmosphere for 1500 h versus that of the control device (86.1%).

Further, the PCE evolution of the unencapsulated devices under operational conditions was recorded to assess the device stability. As shown in Figure 7a, the unencapsulated control device displays a fast degradation and merely retains 40.7% of its initial PCE after continuous light-soaking ( $100 \text{ mW cm}^{-2}$ , without UV light filter) for 500 h under ambient environment (30–40% relative humidity, 25–30 °C) when tracked under MPP condition. Comparatively, the unencapsulated target device featuring comparable PCE as champion device performs much better with 81.9% of its original values being maintained after operating under the same condition (Figure S23 and Table S11, Supporting Information). This significant enhancement for the target device stability against light-soaking should be ascribed to the suppressed  $\text{Li}^+$  ions migration from 1,4-dithiane post-treatment.

Besides, the unencapsulated target device presents stronger humidity endurance with 89.5% of its initial efficiency

being retained after storing at high humidity environment (RH~65%, 25–30 °C) for 500 h vs the control device (55.4%) in Figure 7b, which is mainly ascribed to the enhanced hydrophobicity after 1,4-dithiane post-treatment (Figure S24, Supporting Information). Additionally, the thermal stability of the unencapsulated devices was evaluated at 85 °C for 500 h under ambient environment (RH 30–40%), and the unencapsulated target device can preserve over 75% of its original efficiency, which is much higher than that of the control one ( $\approx 20\%$ , Figure 7c).

Finally, the potential Pb leakage of the unencapsulated device was estimated via inductively coupled plasma-mass spectrometry (ICP-MS) according to the previously reported method.<sup>[56]</sup> It is noticeable that the Pb leakage amount of the control device rapidly increased from 40.1 to 79.3 ppm after light-soaking for 120 h (Figure 7d). In contrast, the target device performs better with remarkably mitigated Pb leakage with only 40.2 ppm Pb ions detected. This greatly reduced Pb leakage concentration of the target device is mainly derived from the significantly enhanced device stability.

### 3. Conclusions

In summary, we have demonstrated the effectiveness of a cost-effective organic molecule 1,4-dithiane in enhancing the performance and stability of PSCs. The introduction of 1,4-dithiane layer between perovskite and HTL could simultaneously

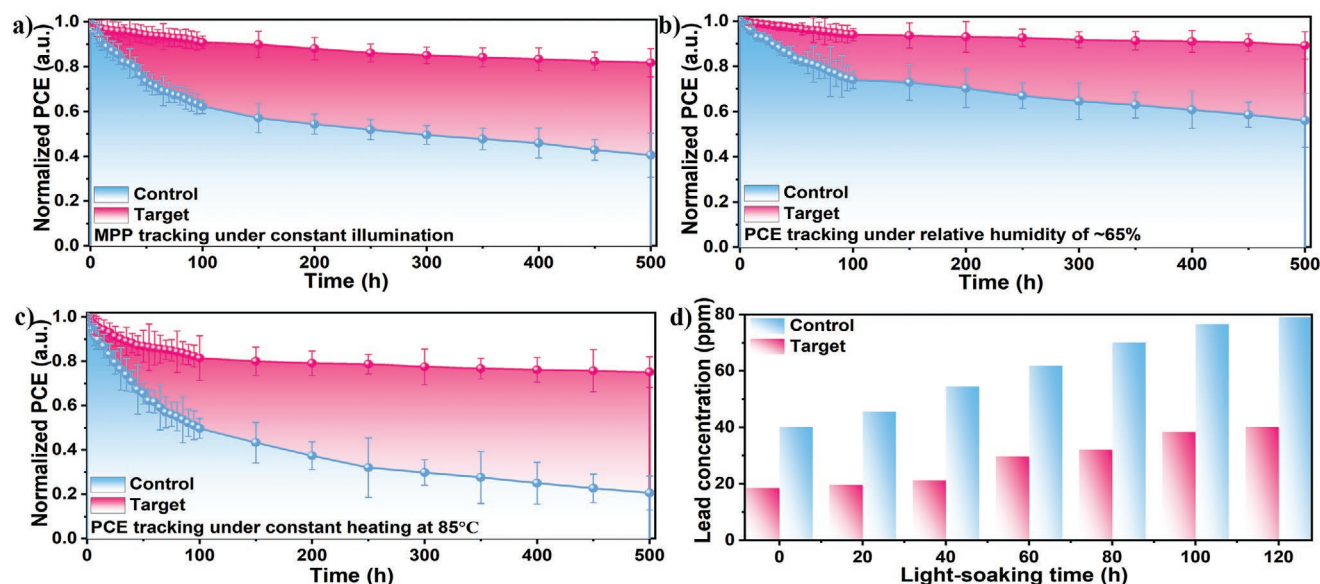


**Figure 7.** Normalized PCE evolution of champion devices after a) constant illumination, b) aging under humid environment, and c) continuous heating for 500 h; d) The leakage amount of  $\text{Pb}^{2+}$  of champion devices after light-soaking for 120 h.

passivate interfacial defects, suppress  $\text{Li}^+$  diffusion, optimize energy level alignment, and increase hydrophobicity of PSCs. Benefiting from those advantages, the target device presents improved charge dynamics with reduced non-radiative recombination, enhanced charge carrier extraction, and improved charge carrier collection. Consequently, the target device shows a promising efficiency of 23.27%. And this facile strategy can be widely adopted for assembling other kinds of high-performance PSCs. Moreover, the appreciably mitigated Pb leakage as well as the significantly enhanced device stability against light-soaking, moisture, and thermal stresses were observed for the target device due to the synergistic suppression of trap-state density, ions migration, and moisture permeation. Our work demonstrates that 1,4-dithiane is a promising candidate for fabricating efficient, stable, and eco-friendly PSCs.

## 4. Experimental Section

Noted that the detailed material source, fabrication process of PSCs, and the characterization of materials and devices are provided in the supporting information.

**Statistical Analysis:** The time-resolved PL, TPV, TPC and device efficiency attenuation under constant illumination, aging under humid environment, and continuous heating in this work were normalized at the apex position. The standard deviation (SD) of PCE histograms based on 34 individual devices for control devices and target devices were 0.63 and 0.39 in Figure S5f, respectively. The normalized PCE evolution under extreme conditions was conducted based on 5 samples. All graphs and data analysis were performed using Excel 2016, Origin Pro2021 software, Avantage, and Adobe Photoshop 2022.

## Supporting Information

Supporting Information is available from the Wiley Online Library or from the author.

## Acknowledgements

X.Q. and C.S. contributed equally to this work. All authors thank the support from the National Natural Science Foundation of China (No. 62204079), the China Postdoctoral Science Foundation (2022M711037), the Leading Talents of Guangdong Province program (2016LJ06N507) and the Shenzhen Basic Research Fund (JCYJ20190809144215761). Meanwhile, the Postgraduate Cultivating Innovation and Quality Improvement Action Plan of Henan University (SYLYC2022184 and SYLYC2022185) provided additional support for this work.

## Conflict of Interest

The authors declare no conflict of interest.

## Data Availability Statement

The data that support the findings of this study are available on request from the corresponding author. The data are not publicly available due to privacy or ethical restrictions.

## Keywords

bidirectional targeted therapies, defects, ions diffusion, perovskite solar cells, stability

Received: December 16, 2022  
Revised: January 18, 2023  
Published online: February 17, 2023

- [1] A. Kojima, K. Teshima, Y. Shirai, T. Miyasaka, *J. Am. Chem. Soc.* **2009**, *131*, 6050.
- [2] J. H. Im, C. R. Lee, J. W. Lee, S. W. Park, N. G. Park, *Nanoscale* **2011**, *3*, 4088.



- [3] H.-S. Kim, C.-R. Lee, J.-H. Im, K.-B. Lee, T. Moehl, A. Marchioro, S.-J. Moon, R. Humphry-Baker, J.-H. Yum, J. E. Moser, M. Grätzel, N.-G. Park, *Sci. Rep.* **2012**, *2*, 591.
- [4] Q. Jiang, J. Tong, Y. Xian, R. A. Kerner, S. P. Dunfield, C. Xiao, R. A. Scheidt, D. Kuciauskas, X. Wang, M. P. Hautzinger, R. Tirawat, M. C. Beard, D. P. Fenning, J. J. Berry, B. W. Larson, Y. Yan, K. Zhu, *Nature* **2022**, *611*, 278.
- [5] N.-G. Park, K. Zhu, *Nat. Rev. Mater.* **2020**, *5*, 333.
- [6] Q. Dong, Y. Fang, Y. Shao, P. Mulligan, J. Qiu, L. Cao, J. Huang, *Science* **2015**, *347*, 967.
- [7] A. Al-Ashouri, E. Köhnen, B. Li, A. Magomedov, H. Hempel, P. Caprioglio, J. A. Márquez, A. B. M. Vilches, E. Kasparavicius, J. A. Smith, N. Phung, D. Menzel, M. Grischek, L. Kegelman, D. Skroblin, C. Gollwitzer, T. Malinauskas, M. Jošt, G. Matič, B. Rech, R. Schlatmann, M. Topič, L. Korte, A. Abate, B. Stannowski, D. Neher, M. Stollerfoht, T. Unold, V. Getautis, S. Albrecht, *Science* **2020**, *370*, 1300.
- [8] N. Chart, <https://www.nrel.gov/pv/cell-efficiency.html>, (accessed: January 2022).
- [9] J. Urieta-Mora, I. Garcia-Benito, A. Molina-Ontoria, N. Martin, *Chem. Soc. Rev.* **2018**, *47*, 8541.
- [10] Z. Li, B. Li, X. Wu, S. A. Sheppard, S. Zhang, D. Gao, N. J. Long, Z. Zhu, *Science* **2022**, *376*, 416.
- [11] Y. C. Yin, Q. Wang, J. T. Yang, F. Li, G. Zhang, C. H. Jiang, H. S. Mo, J. S. Yao, K. H. Wang, F. Zhou, H. X. Ju, H. B. Yao, *Nat. Commun.* **2020**, *11*, 1761.
- [12] H. Zhang, K. Darabi, N. Y. Nia, A. Krishna, P. Ahlawat, B. Guo, M. H. S. Almalki, T. S. Su, D. Ren, V. Bolnykh, L. A. Castriotta, M. Zendejdel, L. Pan, S. S. Alonso, R. Li, S. M. Zakeeruddin, A. Hagfeldt, U. Rothlisberger, A. Di Carlo, A. Amassian, M. Gratzel, *Nat. Commun.* **2022**, *13*, 89.
- [13] J. Xia, Y. Zhang, C. Xiao, K. G. Brooks, M. Chen, J. Luo, H. Yang, N. I. D. Klipfel, J. Zou, Y. Shi, X. Yao, J. Chen, J. M. Luther, H. Lin, A. M. Asiri, C. Jia, M. K. Nazeeruddin, *Joule* **2022**, *6*, 1689.
- [14] L. Chao, T. Niu, Y. Xia, Y. Chen, W. Huang, *Accounts Mater. Res.* **2021**, *2*, 1059.
- [15] D. H. Kim, C. P. Muzzillo, J. Tong, A. F. Palmstrom, B. W. Larson, C. Choi, S. P. Harvey, S. Glynn, J. B. Whitaker, F. Zhang, Z. Li, H. Lu, M. F. A. M. van Hest, J. J. Berry, L. M. Mansfield, Y. Huang, Y. Yan, K. Zhu, *Joule* **2019**, *3*, 1734.
- [16] Q. Fu, H. Liu, X. Tang, R. Wang, M. Chen, Y. Liu, *ACS Energy Lett.* **2022**, *7*, 1128.
- [17] X. Li, W. Zhang, Y. C. Wang, W. Zhang, H. Q. Wang, J. Fang, *Nat. Commun.* **2018**, *9*, 3806.
- [18] L.-L. Jiang, Z.-K. Wang, M. Li, C.-H. Li, P.-F. Fang, L.-S. Liao, *J. Mater. Chem. A* **2019**, *7*, 3655.
- [19] Y. Shen, K. Deng, Q. Chen, G. Gao, L. Li, *Adv. Mater.* **2022**, *34*, 2200978.
- [20] R. Wang, M. Mujahid, Y. Duan, Z. K. Wang, J. Xue, Y. Yang, *Adv. Funct. Mater.* **2019**, *29*, 1808843.
- [21] Y. Liang, P. Song, H. Tian, C. Tian, W. Tian, Z. Nan, Y. Cai, P. Yang, C. Sun, J. Chen, L. Xie, Q. Zhang, Z. Wei, *Adv. Funct. Mater.* **2021**, *32*, 2110139.
- [22] H. Luo, P. Li, J. Ma, L. Han, Y. Zhang, Y. Song, *Adv. Energy Mater.* **2022**, *12*, 2201242.
- [23] H. Zhao, Y. Han, Z. Xu, C. Duan, S. Yang, S. Yuan, Z. Yang, Z. Liu, S. Liu, *Adv. Energy Mater.* **2019**, *9*, 1902279.
- [24] J. Liang, Z. Liu, L. Qiu, Z. Hawash, L. Meng, Z. Wu, Y. Jiang, L. K. Ono, Y. Qi, *Adv. Energy Mater.* **2018**, *8*, 1800504.
- [25] <https://periodictableguide.com/atomic-radius-chart-of-all-elements/2022> (accessed: April 2022).
- [26] T. Imran, S. Rauf, H. Raza, L. Aziz, R. Chen, S. Liu, J. Wang, M. A. Ahmad, S. Zhang, Y. Zhang, Z. Liu, W. Chen, *Adv. Energy Mater.* **2022**, *12*, 2200305.
- [27] J. Zhu, S. Park, O. Y. Gong, C. Sohn, Z. Li, Z. Zhang, B. Jo, W. Kim, G. S. Han, D. H. Kim, T. K. Ahn, J. Lee, H. S. Jung, *Energy Environ. Sci.* **2021**, *14*, 4903.
- [28] S. Wang, F. Cao, P. Chen, R. He, A. Tong, Z. Lan, P. Gao, W. Sun, J. Wu, *Chem. Eng. J.* **2023**, *453*, 139721.
- [29] Q. Zhou, Y. Gao, C. Cai, Z. Zhang, J. Xu, Z. Yuan, P. Gao, *Angew. Chem., Int. Ed.* **2021**, *60*, 8303.
- [30] Z. Guo, S. Zhao, N. Shibayama, A. Kumar Jena, I. Takei, T. Miyasaka, *Adv. Funct. Mater.* **2022**, *32*, 2207554.
- [31] C. Liu, J. Fan, H. Li, C. Zhang, Y. Mai, *Sci. Rep.* **2016**, *6*, 35705.
- [32] S. G. Kim, T. H. Le, T. de Monfreid, F. Goubard, T. T. Bui, N. G. Park, *Adv. Mater.* **2021**, *33*, 2007431.
- [33] Z. Hawash, L. K. Ono, S. R. Raga, M. V. Lee, Y. Qi, *Chem. Mater.* **2015**, *27*, 562.
- [34] S. Wu, L. Liu, B. Zhang, Y. Gao, L. Shang, S. He, S. Li, P. Zhang, S. Chen, Y. Wang, *ACS Appl. Mater. Interfaces* **2022**, *14*, 41389.
- [35] H. Min, J. Hu, Z. Xu, T. Liu, S. U. Khan, K. Roh, Y. L. Loo, B. P. Rand, *Adv. Mater.* **2022**, *34*, 2205309.
- [36] Z. He, C. Zhong, X. Huang, W. Y. Wong, H. Wu, L. Chen, S. Su, Y. Cao, *Adv. Mater.* **2011**, *23*, 4636.
- [37] Y. Gao, M. Cui, S. Qu, H. Zhao, Z. Shen, F. Tan, Y. Dong, C. Qin, Z. Wang, W. Zhang, Z. Wang, Y. Lei, *Small* **2021**, *18*, 2104623.
- [38] J. Huang, S. He, W. Zhang, A. Saparbaev, Y. Wang, Y. Gao, L. Shang, G. Dong, L. Nurumbetova, G. Yue, Y. Tu, *Sol. RRL* **2021**, *6*, 2100839.
- [39] Z. Zhang, F. He, W. Zhu, D. Chen, W. Chai, D. Chen, H. Xi, J. Zhang, C. Zhang, Y. Hao, *Sustainable Energy Fuels* **2020**, *4*, 4506.
- [40] S. Daskeviciute-Geguziene, Y. Zhang, K. Rakstys, G. Kreiza, S. B. Khan, H. Kanda, S. Paek, M. Daskeviciene, E. Kamarauskas, V. Jankauskas, A. M. Asiri, V. Getautis, M. K. Nazeeruddin, *Angew. Chem., Int. Ed.* **2022**, *61*, 202113207.
- [41] J. Song, H. Liu, W. Pu, Y. Lu, Z. Si, Z. Zhang, Y. Ge, N. Li, H. Zhou, W. Xiao, L. G. Wang, M. Sui, *Energy Environ. Sci.* **2022**, *15*, 4836.
- [42] H. Min, D. Y. Lee, J. Kim, G. Kim, K. S. Lee, J. Kim, M. J. Paik, Y. K. Kim, K. S. Kim, M. G. Kim, T. J. Shin, S. I. Seok, *Nature* **2021**, *598*, 444.
- [43] X. Li, Z. Shi, F. Behrouznejad, M. Hatamvand, X. Zhang, Y. Wang, F. Liu, H. Wang, K. Liu, H. Dong, F. Mudasar, J. Wang, A. Yu, Y. Zhan, *J. Energy Chem.* **2022**, *67*, 1.
- [44] J. Hu, C. Wang, S. Qiu, Y. Zhao, E. Gu, L. Zeng, Y. Yang, C. Li, X. Liu, K. Forberich, C. J. Brabec, M. K. Nazeeruddin, Y. Mai, F. Guo, *Adv. Energy Mater.* **2020**, *10*, 2000173.
- [45] Y. Gao, Z. Wang, G. Yue, X. Yu, X. Liu, G. Yang, F. Tan, Z. Wei, W. Zhang, *Sol. RRL* **2019**, *3*, 1900012.
- [46] Y. Gao, Z. Wang, J. Zhang, H. Zhang, K. Lu, F. Guo, Y. Yang, L. Zhao, Z. Wei, Y. Zhang, *J. Mater. Chem. A* **2018**, *6*, 4023.
- [47] S. Wang, L. Tan, J. Zhou, M. Li, X. Zhao, H. Li, W. Tress, L. Ding, M. Graetzel, C. Yi, *Joule* **2022**, *6*, 1344.
- [48] F. Cai, J. Cai, L. Yang, W. Li, R. S. Gurney, H. Yi, A. Iraqi, D. Liu, T. Wang, *Nano Energy* **2018**, *45*, 28.
- [49] S. He, L. Shang, Y. Gao, Y. Shi, F. Tan, X. Chen, G. Yue, *J. Alloys Compd.* **2022**, *896*, 162864.
- [50] X. Gao, Z. Su, S. Qu, W. Zhang, Y. Gao, S. He, Z. Wang, S. Lu, G. Dong, G. Yue, F. Tan, Z. Wang, *J. Mater. Chem. C* **2021**, *9*, 13500.
- [51] Y. Gao, Z. Shen, F. Tan, G. Yue, R. Liu, Z. Wang, S. Qu, Z. Wang, W. Zhang, *Nano Energy* **2020**, *76*, 104964.
- [52] L. Shang, S. Qu, Y. Deng, Y. Gao, G. Yue, S. He, Z. Wang, Z. Wang, F. Tan, *J. Mater. Chem. C* **2021**, *10*, 506.
- [53] L. Shang, W. Zhang, B. Zhang, Y. Gao, S. He, G. Dong, W. Li, H. Bai, G. Yue, S. Chen, F. Tan, *Sol. RRL* **2022**, *6*, 2200605.
- [54] J. Lee, M. Malekshahi Byranvand, G. Kang, S. L. Y. Son, S. Song, G.-W. Kim, T. Park, *J. Am. Chem. Soc.* **2017**, *139*, 12175.
- [55] W. Ke, M. G. Kanatzidis, *Nat. Commun.* **2019**, *10*, 965.
- [56] J. Du, J. Duan, Q. Guo, Y. Duan, X. Yang, Q. Zhou, Q. Tang, *J. Mater. Chem. A* **2021**, *9*, 25418.